



Cite this: DOI: 10.1039/d6ma00041j

# Multimaterial additive manufacturing of GelMA hydrogel-based structures with tuneable composition and mechanical properties

Keyvan Joderi,<sup>a</sup> Silvia Santoni,<sup>b</sup> Charles E. D. Heaton,<sup>a</sup> Feiran Wang,<sup>a</sup> Nathan Carpentier,<sup>b</sup> Long Jiang,<sup>b</sup> Felicity R. A. J. Rose,<sup>b</sup> Ricky D. Wildman<sup>\*a</sup> and Lyudmila Turyanska<sup>ib \*a</sup>

Multimaterial additive manufacturing is an emerging field that could underpin innovation across various industries, with multimaterial hydrogel structures being of particular interest for healthcare. Stereolithography-based processes offer high resolution and compatibility with materials, such as hydrogels. Here, we present a methodology to achieve high resolution multimaterial fabrication of GelMA- and PEG-based hydrogels using vat-photopolymerisation processes, including projection micro-stereolithography and two-photon polymerisation. By optimising resin formulations, printing strategies, and post-printing processes, we produce high-fidelity 3D multimaterial hydrogel structures with either defined material interfaces or compositional gradients, which provide a tool for controllable modification of their chemical composition, alongside tunable mechanical properties (in the range of 2–12 kPa). Using rhodamine B and acrylated rhodamine B, as exemplar guest molecules, we demonstrate reversible impregnation of hydrogels for sustained release and permanent formation of compositional gradients. These capabilities, combined with the inherent biocompatibility of hydrogels, are relevant for applications in drug delivery, wound healing, and environmental sensing, among others. As an illustration, we evaluate the performance of printed hydrogels as sensing layers on interdigitated devices for monitoring salt-rich environments. Together, these findings establish a versatile strategy for high-resolution multimaterial hydrogel manufacturing, offering new opportunities for engineered bio-architectures, suitable for healthcare and environmental applications.

Received 7th January 2026,  
Accepted 15th May 2026

DOI: 10.1039/d6ma00041j

rsc.li/materials-advances

## Introduction

Light-based additive manufacturing (AM) processes, particularly vat-photopolymerization, are widely recognised for their ability to generate complex customizable geometries with high resolution using a range of materials from polymers,<sup>1,2</sup> ceramics<sup>3</sup> and glasses<sup>4</sup> to hydrogels.<sup>5,6</sup> While these capabilities already enable notable advancements in diverse areas from bioelectronics<sup>7</sup> and healthcare<sup>8</sup> to quantum technologies,<sup>9</sup> there is a strong need for material formulations and multimaterial AM,<sup>10</sup> to produce structures with both smooth and stepped compositional gradients, for applications from sensing and robotics to tissue engineering.<sup>11</sup> Switching from single

material to multimaterial AM requires the development of compatible resins and an understanding of underlying mechanisms governing material interfaces.<sup>12</sup> Among the materials available for vat-photopolymerization processes, hydrogels have attracted significant attention due to their high-water content, water-filled polymer porous network structure and biocompatibility,<sup>13–15</sup> making them attractive for bioprinting applications, biomedical engineering, soft robotics, environmental sensing, *etc.*<sup>16</sup>

The properties of printed hydrogels can be tailored by printing parameters to achieve different degrees of polymerization and composition, allowing for precise control of the functional characteristics of the final structure.<sup>17</sup> Among natural, synthetic and hybrid hydrogels, gelatine and polyethylene glycol (PEG) derivatives are the most commonly used due to their availability, suitability for AM-based processes, tuneable mechanical properties, permeability and biocompatibility.<sup>18</sup> Inherent porosity of hydrogels was successfully used to produce intricate designs by infusion<sup>19</sup> and has been developed for applications ranging from sensing<sup>20</sup> to controlled drug

<sup>a</sup> Centre for Additive Manufacturing, Faculty of Engineering, University of Nottingham, NG7 2RD, Nottingham, UK.  
E-mail: Ricky.Wildman@nottingham.ac.uk,  
Lyudmila.Turyanska@nottingham.ac.uk

<sup>b</sup> School of Pharmacy, Nottingham Biodiscovery Institute, Faculty of Science, University of Nottingham, Nottingham, NG7 2RD, UK



delivery.<sup>21</sup> Significant advantages can be achieved by combining tuneable properties of hydrogels and advancements demonstrated for single material structures with multimaterial designs with the potential to produce property gradients, enabling manufacturing of parts that mimic their surrounding or respond to their environment. Use of hydrogels in multimaterial designs was recently demonstrated in inkjet-printed and extrusion-manufactured structures.<sup>22–24</sup> Vat-based processes offer opportunities for the manufacturing of designs with a high degree of geometrical freedom with sizes up to tens of centimetres and with resolution down to the sub-micron scale enabled by multi-photon polymerization printing.<sup>25</sup> Tailoring of the material properties was achieved through grayscale polymerization strategies,<sup>26</sup> controlled reaction diffusion<sup>27</sup> and by the use of different excitation wavelengths.<sup>28</sup> To achieve multimaterial designs, sequential resin exchange is considered promising and is attracting increasing research efforts. While successes of all these approaches are notable, reports on fully hydrogel-based multimaterial designs and strategies to achieve high resolution printing with compositional gradients are still limited.

Here we report a methodology to achieve high resolution multimaterial printing of hydrogels. We establish the resin composition, printing parameters and post deposition strategies to produce structures with either defined stepped multimaterial sections or with smooth compositional gradients, which can be used to provide a tool for tuning the chemical composition and mechanical properties of the printed designs. We demonstrate multimaterial printing of hydrogels with high-resolution, high shape definition and mechanical properties tuneable by printing parameters. The resin formulations are printable on different manufacturing platforms from projection microstereolithography (resolution 10  $\mu\text{m}$ ) to multiphoton polymerization (sub-micron resolution). The hydrogel porosity enables impregnation of the structures with guest molecules to achieve gradients of composition. By using rhodamine dye and acrylated rhodamine dye as exemplar molecules, we demonstrate that reversible impregnation can be achieved enabling sustained release of a guest molecule, and that permanent compositional gradients can be produced in these hydrogels, respectively. Our work provides a strategy for both in-process and post-printing programming of compositional and mechanical properties, either with smooth or stepped gradients. These properties, combined with the biocompatibility of hydrogels, are of interest for a range of applications, including drug delivery systems, tissue engineering, and environmental sensing. To illustrate this, we investigate the performance of printed hydrogels as a sensing layer on interdigitated devices for sensing salt-rich environments.

## Experimental methods

### Materials

Acryloxyethyl thiocarbonyl rhodamine B was purchased from Polysciences. 4-Arm PEG-acrylate (molecular weight 20 000 Da)

was obtained from Laysan Bio, Inc. PEG dithiol (SH-PEG-SH, molecular weight 2000 Da) was acquired from Creative PEG-Works. Lithium phenyl(2,4,6-trimethylbenzoyl)-phosphinate (LAP) was sourced from Tokyo Chemical Industry. Tartrazine, gelatin from porcine skin with a gel strength of approximately 175 g Bloom (Type A), methacrylic anhydride (MA), ethanol, and 3-(trimethoxysilyl)propyl methacrylate (TMSPMA) were all purchased from Sigma-Aldrich. All chemicals were used without any further purification.

### GelMA synthesis and chemical characterization

Gelatin type A (Merck) was modified *via* a method adapted from Kim *et al.*<sup>29</sup> Briefly, gelatin (10.0 g) was dissolved in 100 mL of deionized water and mixed with 40 g of MA and 3 g of TEA. The reaction mixture was kept for three days at 60 °C, then the solution was precipitated twice in excess of ethanol (20 $\times$  reaction volume), filtered, dried in a vacuum (12 hour, room temperature), and dialyzed for three days against deionised water. The solution was lyophilized for two days to generate a white powder and was stored at  $T = -20$  °C. GelMA NMR spectra confirmed successful modification (supplementary information, SI, Fig. S1).

### Hydrogel formulations

Different concentrations of GelMA (10, 20, and 30 w/v%) were prepared by dissolving lyophilized GelMA in deionized water or PBS. Lithium phenyl(2,4,6-trimethylbenzoyl)phosphinate (LAP) or tetrapotassium 4,4'-(1,2-ethenediyl)bis[2-(3-sulfophenyl)diazene-sulfonate] (DAS) was used as a photoinitiator, at a final concentration of 1% w/v and 1 mM respectively. For microstereolithography, 0.025% of tartrazine was added as a photoabsorber.

A 4Arm-PEG-Ac formulation was prepared by mixing 10% w/v 4-Arm PEG-Acrylate (4Arm-PEG-Ac) and PEG dithiol (SH-PEG-SH) in a 2:1 molar ratio, 0.025% w/v tartrazine as a photoabsorber, and 1% w/v LAP as a photoinitiator, and deionized water at room temperature. The mixtures were stirred continuously for one hour to ensure complete dissolution.

### Glass silanisation

To avoid detachment of the photocured hydrogel, the glass coverslip surface was functionalised with methacrylate and used as a printing platform. To perform methacrylation, the glass coverslip was placed on a platform wrapped with aluminium foil into the plasma chamber. The pressure inside the chamber was lowered to 0.18 mbar and the power set to 50 W. The glass coverslips were treated with O<sub>2</sub> plasma for 10 minutes. The activated glass coverslips were dipped into toluene with 2% (w/w) TMSPMA for one hour at 50 °C, followed by three cycles of washing with acetone, dried under nitrogen, and stored in a vacuum at 35 °C.

### Additive manufacturing

For each resin/printer, a processability window was systematically assessed by printing an array of cubic structures using varying values of laser power and speed (see SI SI1, SI2 for



details). A projection micro-stereolithography ( $\mu$ SLA) system (nanoArch S240, Boston Microfabrication (BMF) Precision Technology Inc., equipped with a UV laser (405 nm)) was used to fabricate 3D structures. LumenX+ was used to produce GelMA hydrogel with a BCC lattice (exposure time 5 s; temperature 35 °C; light intensity 55%; layer height 100  $\mu$ m). 3D models were designed using Fusion360 software, then sliced with BMF slicing software to obtain a layer height of 10  $\mu$ m. Each layer was exposed to irradiation for 2 s, with a delay time of 4 s. Post-printing, the samples were rinsed, and stored in water at  $T = 8$  °C.

A 2-photon polymerisation (2PP) system (NanoOne printer, Think3D software (UpNano GmbH)) was used to print micron-scale structures using the bottom-up mode with a 10 $\times$  objective (UPLXAPO10X, NA 0.4, Olympus) at the machine operating temperature ( $\sim 28$  °C).<sup>30</sup> The processability window for 2PP was assessed by printing an array of 100  $\mu$ m  $\times$  100  $\mu$ m  $\times$  100  $\mu$ m cubes and lattice structures (cell dimension: 20  $\mu$ m). In the array, the power and printing speed were varied between 25 and 300 mW and 100 and 800 mm s<sup>-1</sup>, respectively, while the layer height and the hatching distance were set at 1  $\mu$ m.

The geometrical swelling of the cubes was measured and the printing parameters that produced minimal swelling were judged to be optimal. The STL of the crypt honeycomb structure was designed using Fusion 360 (Autodesk Inc.), to obtain a model with dimensions of 1000  $\mu$ m  $\times$  1000  $\mu$ m  $\times$  300  $\mu$ m.

### Morphological and mechanical characterization

The optical microscopy images were acquired using an optical microscope (Nikon Eclipse LV100ND). AFM indentation was carried out on the MFP-3D AFM (Asylum Research) using an MLCT-A AFM tip (Bruker). The spring constant of the cantilever was calibrated to be 0.1042 N m<sup>-1</sup>. The indentation depth was 1.8  $\mu$ m and the indentation velocity was 5  $\mu$ m s<sup>-1</sup>. The deflection sensitivity of the tip in air was first obtained by indentations on a fused silica surface. The spring constant of the tip was then obtained using the Thermal Tune method. Indentation experiments were performed in DI water. The deflection sensitivity of the tip in water was calibrated by indentations on a glass slide in DI water. For each sample, 3 regions were examined with 24 indentations performed at varied locations in each region. The Young's modulus was then calculated from force–distance curves using the DMT (Derjaguin–Muller–Toporov) theory with a conical tip geometry model.<sup>31</sup> The equivalent tip half conical angle is around 19° according to the tip specifications. Samples used for this study were either washed immediately after printing to remove the photoinitiator (3 times with deionised water) or were post-cured under UV exposure (Anycubic Wash and Cure Machine 2.0, 10 mW cm<sup>-2</sup>, 405 nm) before washing.

For confocal microscopy imaging, the printed structures were incubated in PBS at 37 °C for 10 min, then washed three times with PBS and kept hydrated in PBS. Prior to imaging, the structures were stained with 1 mg ml<sup>-1</sup> rhodamine B in PBS and were sliced to a thickness of 250  $\mu$ m using a Leica VT1200. Imaging was performed using a confocal microscope (Leica

TCS SPE, Leica Microsystems). Images were analysed using Fiji/ImageJ and MATLAB R2023b (MathWorks, Natick, USA) scripts.

### Printed sensing device

Graphene/PEDOT:PSS ink (Sigma-Aldrich) was used as received and interdigitated electrodes were printed on a piezo-driven Fujifilm Dimatix DMP-2800 inkjet printer using 2.4 pL drop volume Dimatix Samba cartridges with 10  $\mu$ m drop spacing. The printer was paused for 30 s between printing each layer to allow for drying, and the nozzles were purged before printing each layer and periodically during printing (for 0.1 s every 100 printed swaths) to achieve consistent jetting. Capacitance measurements were performed using a Rohde & Schwarz Hameg HM8118 programmable LCR bridge.

The hydrogels used in this work were formulated from thiolated gelatine (5 w/v%), norbornene-modified gelatine (5 w/v%) and 0.5 w/v% lithium phenyl (2,4,6-trimethylbenzoyl) phosphinate (LAP) dissolved in phosphate-buffered saline (PBS). The hydrogels were printed using an Elegoo Mars 4 SLA printer into cubes with dimensions of 5  $\times$  5  $\times$  5 mm.

### Statistical analysis

All data reported in the manuscript are presented as averages with standard deviations from at least 3 repeats. Specific information is provided in the data caption.

## Results and discussion

To develop high resolution additive manufacturing of multi-material hydrogel structures, the following materials were formulated as resins for  $\mu$ SLA: gelatin methacryloyl (GelMA),<sup>29</sup> GelMA with acrylated rhodamine B (GelMA/rhodamine B), and 4Arm-PEG and 4Arm-PEG with acrylated rhodamine B (4Arm-PEG/rhodamine B) (Fig. 1a). To produce hydrogel multimaterial structures, a photostereolithography process is used with acrylated resins. Part of the sample is printed in a vat filled with one material resin, which is then replaced with other resin to complete the print (Fig. 1b). Acrylated rhodamine B was selected for this work as a fluorescent dye to enable visual demonstration and confocal imaging of multimaterial structures and to observe the in-diffusion of guest molecules.

By optimising printing parameters, such as laser power and layer depth, all resins were printed into high fidelity structures, either as individual hydrogels or as heterostructures. To produce the latter, the printing conditions are such that cross polymerization at the interface of two materials is possible, ensuring that there is no de-lamination. To refine the photocurable resin formulation for successful hydrogel crosslinking,<sup>32</sup> GelMA was prepared with concentrations of 10, 20, and 30%w/v into cubic 5 mm  $\times$  5 mm  $\times$  3 mm structures on  $\mu$ SLA (power  $P = 20$  mW cm<sup>-2</sup>, exposure time 2 s). With increasing GelMA concentration, the definition of the printed shapes improved and high fidelity structures were printed with 30% GelMA (Fig. 1c, and Fig. S2), as expected for the higher density material.<sup>33</sup> The formulation with GelMA 20 w/v% also has good printability, as demonstrated



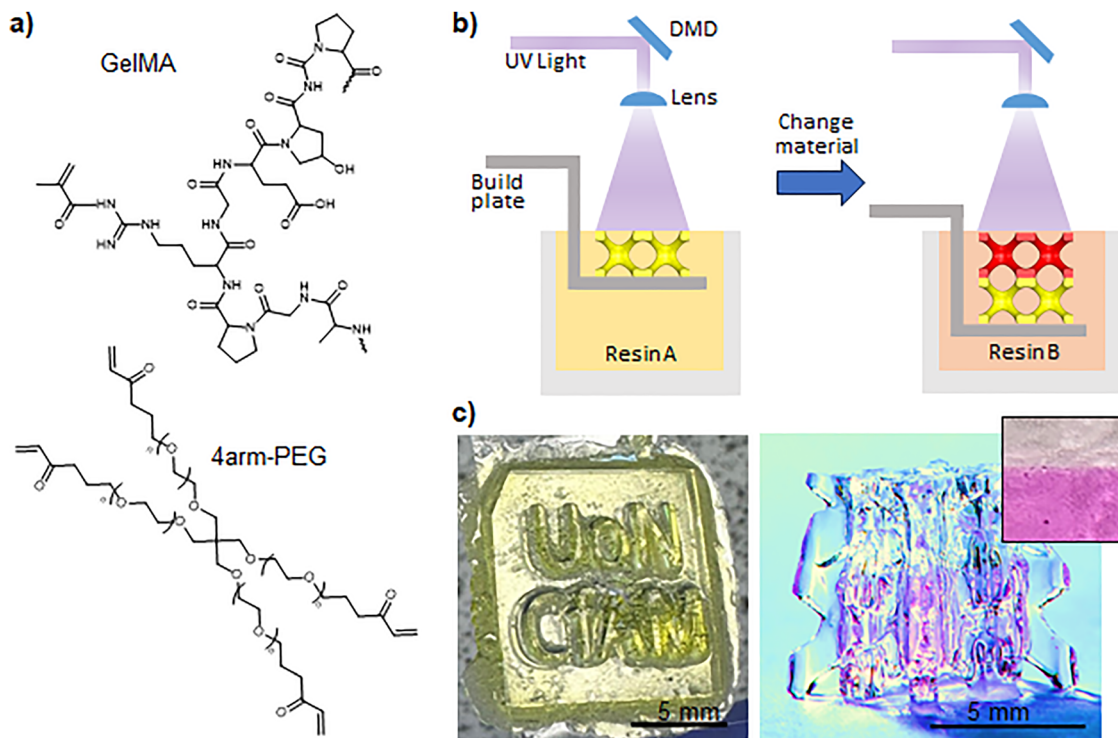


**Fig. 1** Hydrogel printing. (a) Chemical structure of GelMA and 4Arm-PEG-Ac. (b) Schematic illustration of a high-resolution projection stereolithography ( $\mu$ SLA) process for multimaterial fabrication. (c) Photographs of the GelMA structure with the University of Nottingham Centre for Additive Manufacturing acronym (left) and GelMA (top) and GelMA/rhodamine B (bottom) multimaterial structures printed into a BCC lattice structure (right), with the inset showing a magnified optical image of the multimaterial interface.

by body-centred cubic (BCC) multi-material lattice structures (overall size of  $1 \times 1 \times 1$  cm with the pink lower part produced using GelMA/rhodamine B, and the top transparent part produced using GelMA Fig. 1c) and demonstrated structural integrity over at least 1 month when stored immersed in water at  $T = 8^\circ\text{C}$ .

The resolution limits achievable depend on both resin formulation and printing parameters. The arrays of nine cylindrical cavities with a diameter of  $85\ \mu\text{m}$  and a depth of  $500\ \mu\text{m}$  structure (Fig. 2a) were printed using GelMA and GelMA with acrylated rhodamine B (GelMA/rhodamine B, 0.001w/v%). Optical images and fluorescent microscopy analysis of these structures revealed that the diameter of the cavity was proportional to the laser power used (Fig. 2b), and decreased from  $\sim 94\ \mu\text{m}$  to  $\sim 52\ \mu\text{m}$  with light power increasing from  $P = 7\ \text{mW cm}^{-2}$  to  $38\ \text{mW cm}^{-2}$ . At higher laser power used, the definition and shape of the cavity at the bottom of the structure were affected by over-polymerization, with some blurring of the edges (Fig. S3). For the cavity arrays produced with lower laser power ( $14\ \text{mW cm}^{-2}$ ), the cylindrical cavities were successfully formed with the intended diameter of  $85 \pm 3\ \mu\text{m}$  throughout the  $500\ \mu\text{m}$  depth of the structure (inset in Fig. 2b). A honeycomb design with smaller feature sizes ( $20\ \mu\text{m}$  walls and  $85\ \mu\text{m}$  cavities with  $500\ \mu\text{m}$  depth) was also successfully printed with lower light power ( $P = 14\ \text{mW cm}^{-2}$ , Fig. 2c) and its geometrical accuracy was confirmed with optical microscopy and fluorescent microscopy, revealing the wall thickness of  $20 \pm 3\ \mu\text{m}$  and

cavity diameter of  $85 \pm 2\ \mu\text{m}$  throughout the  $500\ \mu\text{m}$  layer thickness. To demonstrate  $20 \pm 3\ \mu\text{m}$  features, which correspond to 2 pixel sizes ( $10\ \mu\text{m}$ ), adjustment of the slicing process was needed to eliminate ‘smoothing’ of the shapes (see SI S1). Although the walls are well defined, there is some pixilation observed, as expected for voxel-by-voxel printing and small feature (2 voxels). The resolution achieved here surpasses that typically demonstrated for GelMA-based prints, with resolution down to  $50\ \mu\text{m}$  only.<sup>34,35</sup> The printing strategies developed for  $\mu$ SLA here can be applied also to 2PP, with the advantage of enhancing printing resolution down to sub-micron values.<sup>36</sup> To demonstrate the compatibility of the resins with the high resolution multiphoton stereolithography process, GelMA formulations ( $20\ \text{w/v\%}$  and  $10\ \text{w/v\%}$ ) were printed on a 2-photon polymerization (2PP) printer, producing high-fidelity honeycomb designs with no visible pixilation (Fig. 2d and Fig. S5 and S6) and the cavity sizes of  $75 \pm 2\ \mu\text{m}$  and wall thickness of  $29 \pm 1\ \mu\text{m}$ . Importantly, the observed definition of the printed walls is sharp, with no blurring observed in fluorescent images. All printed GelMA structures were stable for at least 1 month of storage at  $8^\circ\text{C}$ . We note that this approach was successfully used for printing of GelMA, GelMA/rhodamine B and 4Arm-PEG resins.

The used printing parameters can provide a route to tune the mechanical properties of hydrogel structures. For example, with increasing light intensity from  $14$  to  $28\ \text{mW cm}^{-2}$ , the Young’s modulus of printed 4Arm-PEG-Ac hydrogels



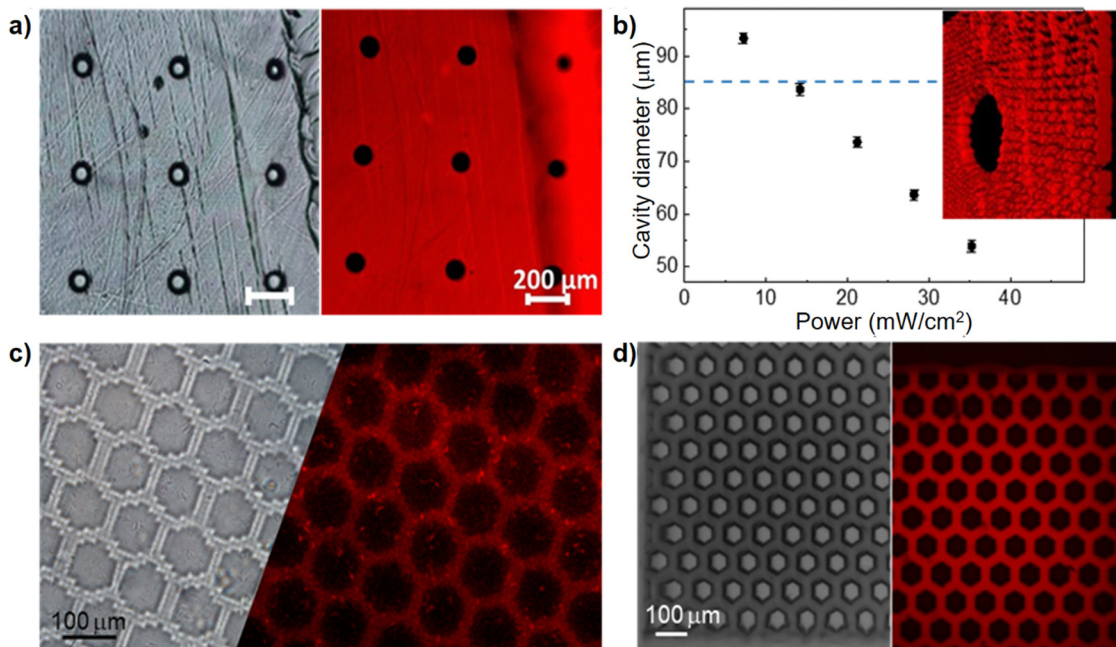


Fig. 2 (a) Optical microscopy and fluorescence microscopy images of a GelMA/rhodamine B structure with a cavity diameter of 85  $\mu\text{m}$  and a depth of 500  $\mu\text{m}$ . (b) Dependence of the cavity diameter on UV power density,  $P$ , used during printing. (Inset) High resolution fluorescent image of the tilted structure ( $P = 14 \text{ mW cm}^{-2}$ ). Error bars represent standard deviation of the measured value based on at least three independent repeats. Representative optical microscopy and fluorescence microscopy images of honeycomb structures printed with GelMA 20 w/v% on (c)  $\mu\text{SLA}$  and (d) on a 2PP printer.

(10%,  $2 \times 2 \times 0.5 \text{ mm}$ ) increased from 2 to 6 kPa (Fig. 3a), and further increased to 12 kPa with additional post-curing (UV 405 nm, 60 s). These results are corroborated with rheology measurements, showing increased stiffness of the hydrogels produced with higher light power, reaching a value of  $\sim 5 \text{ kPa}$  for samples printed with  $P = 28 \text{ mW cm}^{-2}$  compared to  $\sim 2.1 \text{ kPa}$  with  $P = 14 \text{ mW cm}^{-2}$  (Fig. 3b). Our statistical analysis using the Kruskal–Wallis test (Fig. S4) revealed that the Young's moduli of all sample pairs show significant differences (excluding two pairs: 14 and 21  $\text{mW cm}^{-2}$ , and 21  $\text{mW cm}^{-2}$  30 s post cure). Post-printing UV curing was used to increase the degree of polymerization in the printed structures, and an increase in stiffness up to  $\sim 6 \text{ kPa}$  was achieved with post-printing UV curing

times of 60 s. We note that the two used methods offer complementary information about the sample, with AFM-derived moduli providing accurate information about the local properties of the surface (within the area of few  $\mu\text{m}^2$ ), and the bulk rheology measurements assessing the (shear) storage modulus representing the macroscopic properties of the structure. While the measured properties are different, it is expected that the trends observed in the two methods are comparable, as we demonstrate in our work. Similar trends were observed for GelMA. The tunability of mechanical properties could open up interesting avenues, particularly for tissue engineering applications, where scaffold stiffness can influence cell behaviour and cell differentiation.<sup>37</sup>

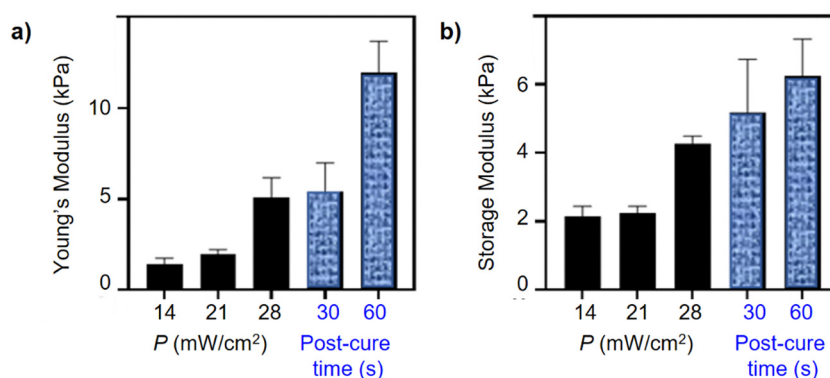


Fig. 3 (a) Young's modulus (AFM measurements) and (b) storage modulus (rheometer measurements) of 4Arm-PEG-Ac hydrogels (10% 4Arm-PEG-Ac, 0.025% tartrazine, and 1% LAP) printed with different light power and following post curing. Error bars represent standard deviation of at least three measurements taken at different areas of the sample.



The printing strategy developed for high resolution printing of individual materials was applied to multimaterial hydrogel designs (Fig. 4). In this process, following printing of the first material, the vat was replaced with the second material resin. A number of different combinations of hydrogels were produced within one structure (Fig. 4a), including GelMA and GelMA/rhodamine B, 4Arm-PEG and 4armPEG/rhodamine B, as well as the combination of distinctly different materials, such as GelMA and 4Arm-PEG-Ac. The swelling degree (SD) of 3D-printed GelMA hydrogels was analysed by immersing the printed cubic structures into water at ambient temperature (Fig. S5). GelMA structures undergo rapid swelling, achieving maximum dimensional expansion of  $SD = 145\%$  within the first hour, with no further expansion detected even after prolonged immersion ( $>12$  hours). The structures composed of 4Arm-PEG-Ac hydrogels exhibited slower swelling reaching  $SD \sim 80\%$  after two-hour immersion. This difference can be attributed to the hydrophilic nature of GelMA, which allows it to absorb more water and swell faster than more hydrophobic 4Arm-PEG-Ac.<sup>38</sup> Importantly, no delamination was observed after washing the printed multimaterial hydrogels, despite differences in swelling of the gels, indicative of chemical bonding and polymerization at the material interface. In resins containing acrylated rhodamine B, the dye was retained in the structure even after excessive washing, providing a qualitative indication that the photopolymerization process leads to a chemical bonding between the monomer and dye. While testing adhesion at the hydrogel interfaces is not possible using conventional tests, in this work we confirmed the structural stability of the multi-material hydrogels using dehydration/rehydration cycles. No indication of delamination was observed, further

indicating the presence of chemical binding between the layers that provided structural stability at the interfaces.

In contrast, the tartrazine used as a photo-absorber was successfully washed out of the gels, including complex 3D hydrogel structures, as evident from the fully transparent and red parts in the gels, with a well-defined boundary (Fig. 4a and b). Successful removal of the photoinitiator and photo-absorber is important for gels considered in healthcare devices, as these materials could be cytotoxic.<sup>39</sup> On the other hand, the porous structure of the hydrogel enables loading and release of guest molecules, which could be of interest for drug delivery and sensing.<sup>40,41</sup>

The ability of hydrogels to absorb and release the molecules (solvent and/or guest molecules) due to high porosity of the structure offers an interesting opportunity for impregnation of hydrogels with guest molecules. The diffusion of guest molecules in hydrogels can occur through the hydrated polymer network, which behaves as a water-rich continuous phase. GelMA and 4Arm-PEG-Ac cuboids ( $5 \times 5 \times 10$  mm) placed on a layer of rhodamine B solution ( $1 \text{ mg mL}^{-1}$ ) (Fig. 5a) initially developed a clear gradient of colour, which was saturated to the top of the structure within three hours (up to the height of 8 mm). Since this process is driven by in-diffusion, the formed structures have a smooth gradient of composition. To qualitatively assess the in-diffusion, image analysis assuming one-dimensional Fickian diffusion and constant boundary concentration was used to determine the diffusion coefficient. The temporal evolution of the diffusion front (analysed by colour intensity) was fitted using Fick's second law for one-dimensional diffusion from a constant-concentration boundary, where the diffusion length  $L = \sqrt{2Dt}$ , with diffusion coefficient  $D = 7.5 \times 10^{-6} \text{ cm}^2 \text{ s}^{-1}$  for rhodamine B, comparable to the expected value

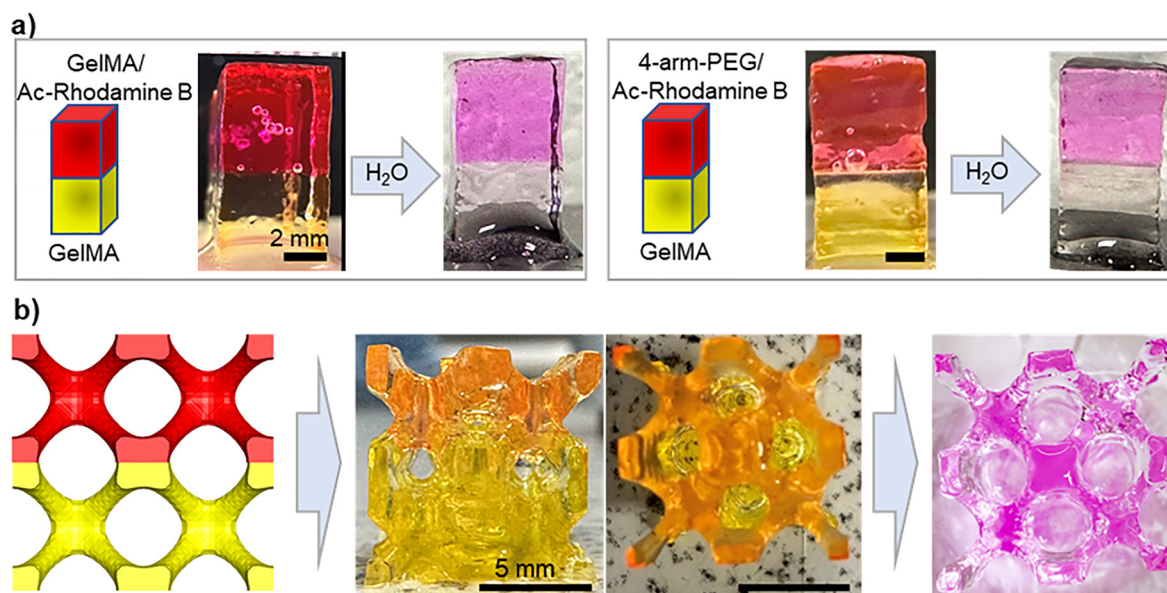


Fig. 4 Multimaterial hydrogel printing. (a) Sketches and photographs of the as-printed multimaterial structures and after washing with water. (Left) GelMA and GelMA with acrylated Ac-rhodamine B dye and (right) GelMA and 4Arm-PEG/Ac-rhodamine B. (b) Design of the multimaterial BCC lattice and photographs of the printed GelMA and GelMA/Ac-rhodamine B structure before (middle) and after (right) washing.



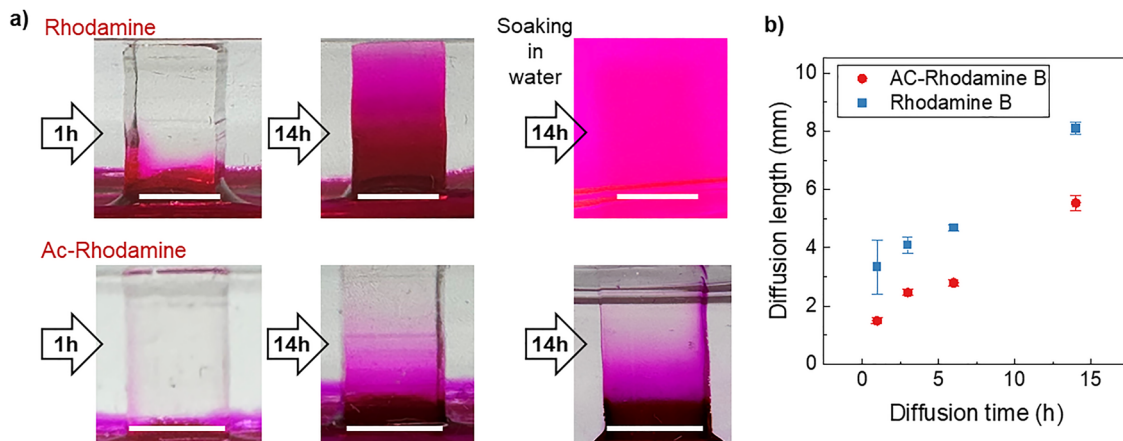


Fig. 5 (a) Optical images of GelMA cubes (5 mm × 5 mm × 10 mm; 20% GelMA, 14 mW cm<sup>-2</sup>) following in-diffusion of rhodamine B and acrylated Ac-rhodamine B for 1 h (left images) and 14 hours (middle images), and after overnight (14 h) soaking in water (right images). Scale bar (1 cm) is placed at the bottom of the gel. (b) Change of diffusion length over time. At least 3 replicates of each sample were used and error bars represent standard deviation of at least 3 measurements.

on water ( $2.8 \times 10^{-6} \text{ cm}^2 \text{ s}^{-1}$ ),<sup>42</sup> which confirms the diffusion driven impregnation process. We note that spatial resolution is limited by optical imaging, and therefore the extracted diffusion coefficient represents an effective macroscopic diffusion coefficient rather than a molecular self-diffusion value. This process is significantly slower for acrylated rhodamine B, reaching the maximum height of  $\sim 5$  mm after overnight exposure (Fig. 5a). The acrylated rhodamine B can react with unreacted methacrylate on GelMA leading to irreversible impregnation of GelMA with rhodamine B. Indeed, following overnight ( $\sim 14$  h) soaking in water, out-diffusion of non-acrylated rhodamine B was observed as evident from the change of the colour of water (top right image in Fig. 5a). In contrast, no noticeable change in the colour of the water and gel was observed after over 14 h of soaking, suggesting that all dye is retained in the hydrogel. This approach can provide a route for post printing functionalisation of hydrogels, enabling formation of permanent smooth gradients of composition, as well as loading of hydrogels with (photo)-sensitive

materials such as biomolecules and peptides, which are not compatible with the printing process or are prone to degradation during storage.

Biocompatibility of hydrogels makes them of interest for healthcare devices. In this application, the ability of hydrogels to exchange substances with the environment offers an opportunity to use them as a functional layer of electronic devices. Monitoring of salts in physiological fluids is of particular interest as it reflects the fluid balance indicative of health changes.<sup>43,44</sup> AM across manufacturing platforms has attracted attention recently and could advance the development of innovative healthcare devices. Here we use inkjet-printed graphene/PEDOT:PSS interdigitated electrodes (IDE) to detect the presence of salts in the surrounding solvent. Soaking of hydrogel in aqueous NaCl solutions (0, 0.1 M, and 1.0 M) leads to in-diffusion of salt ions into the gels (Fig. 6). Hence, the capacitance of the IDE surface decorated with a hydrogel layer changes in response to the quantity of ions present in the gel,

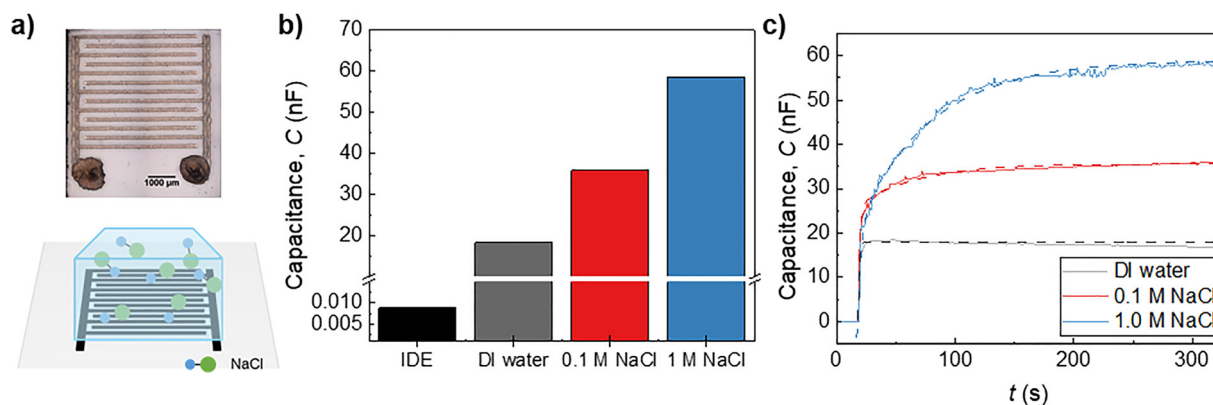


Fig. 6 (a) Optical image of Gr/PEDOT:PSS IDE and schematic of the device with the NaCl hydrogel placed on top for capacitance sensing. (b) Maximum capacitance value achieved when depositing hydrogel and NaCl-soaked hydrogels onto the Gr/PEDOT:PSS interdigitated electrode (IDE). (c) Temporal response of the IDE to exposure to GelMA and NaCl-soaked GelMA. Dashed lines represent exponential fitting of the experimental data.



which is proportional to the concentration of salt. The capacitance of naked IDE is  $C_{\text{no-hydrogel}} = 8.8$  pF, which increased to  $C_{0\text{M}} = 18.2$  nF for the device decorated with a  $1 \times 1 \times 1$  cm cube of GelMA. This change in measured capacitance is due to the change of the permittivity and electrolytic conductivity of the medium in direct contact with its electrode fingers, so the change from air to hydrogel results in an increase of capacitance.<sup>45,46</sup> Following soaking in 0.1 M, 1.0 M solutions of NaCl, the capacitance and response time increase to  $C_{0.1\text{M}} = 35.8$  nF,  $t_{0.1\text{M}} \sim 50$  s and  $C_{1\text{M}} = 58.5$  nF,  $t_{1\text{M}} = 62$  s, respectively.

While this work focussed on developing the hydrogels, the results demonstrate not only the potential of printed hydrogels as a sensing medium, but also an opportunity of cross-AM platform manufacturing. Our work demonstrates the feasibility of forming permanent functional gradients both in printing and post-printing. We propose that this approach is transferable to other molecules, with functional groups capable of photopolymerization (*i.e.* acrylate) to achieve permanent loading of 3D printed hydrogels. We envisage that the degree and time of loading will be size-dependent and can be controlled by diffusion rate. The printability of the same hydrogel formulation across different AM platforms, as well as the multi-material 3D printing of different types of resins (GelMA based as well as GelMA-4Arm-PEG), can be used as a strategy for on-demand manufacturing of designs incorporating softer (GelMA) and more mechanically robust and structurally stable 4Arm PEG, particularly beneficial for tissue engineering applications.<sup>47</sup> Biocompatibility of hydrogels is well reported, however unpolymerized monomers and photoinitiators could induce biotoxicity.<sup>48,49</sup> In this work, we demonstrated that excessive washing can be performed to remove photoinitiators (Fig. 1 and 2) and small molecules (Fig. 4), and we envisage that small monomers can be also removed. Additionally, post printing UV curing provides a route to increase the degree of polymerization, thereby reducing the amount of unpolymerized functional groups. Our preliminary assessment of biocompatibility of printed structures was performed using a live-dead assay on the fibroblast-like cell line L929 exposed for 24 h to GelMA (up to 10%), with optical images revealing no noticeable changes in cell density or cell morphology, and with cell viability higher than 70% (SI, SI3). However, the biocompatibility studies merit further detailed investigations, including the exploration of the effect of hydrogel design on cell proliferation. The results reported here, in combination with developments of resins for hydrogel printing, particularly multimaterial hydrogels, have the potential to underpin their future adoption in tissue engineering and bioprinting.

## Conclusions

We developed resin formulations and printing strategies to produce hydrogels with controlled and tuneable compositions and properties. Our multimaterial printing enables manufacturing of hydrogel structures with defined material interfaces,

yet integrated into a consolidated structure with a high degree of geometric complexity. The in-diffusion based approach that we demonstrated provides a route to impregnate the hydrogels with guest molecules in both a permanent and reversible manner, and with opportunities to form a gradient of concentration. We demonstrated that our approaches can be used with different hydrogels, including GelMA and 4Arm-PEG-Ac hydrogels. This work demonstrates the use of light-based additive manufacturing approaches to produce multimaterial 3D hydrogel structures with high resolution, and opportunities for the creation of gradients of chemical and mechanical properties. The reported results could inform and enable the development of innovative healthcare devices for biosensing, diagnostics, tissue engineering, and regenerative medicine, as well as for environmental sensing.

## Author contributions

KJ, SS, CH, FW, NC and LJ performed experimental studies. All co-authors contributed to conceiving of the project, data analysis, funding acquisition, project supervision and manuscript writing.

## Conflicts of interest

The authors declare no known competing interests.

## Data availability

All data used in this work are reposted in the manuscript and in the supplementary information (SI). Supplementary information is available and includes informations on resin formulations and characterization studies; two-photon manufacturing; and preliminary biocompatibility studies. See DOI: <https://doi.org/10.1039/d6ma00041j>.

Additional data can be obtained from the corresponding author upon reasonable request.

## Acknowledgements

This work was funded by the Engineering and Physical Sciences Research Council [grant numbers EP/W017032/1 and EP/P031684/1]. The authors acknowledge access to the nmRC facilities and assistance with Raman spectroscopy from Dr Graham Rance, Dr Tim Self for assistance with fluorescence microscopy, and Dr Peng Zhao for useful discussions.

## References

- 1 A. Randhawa, S. D. Dutta, K. Ganguly, D. K. Patel, T. V. Patil and K. Lim, *Macromol. Biosci.*, 2023, **23**, 2200278.
- 2 A. Dominguez-Alfaro, E. Mitoudi-Vagourdi, I. Dimov, M. L. Picchio, N. Lopez-Larrea, J. L. de Lacalle, X. Tao, R. R. Serrano, A. Gallastegui, N. Vassardanis, D. Mecerreyes and G. G. Malliaras, *Adv. Sci.*, 2024, **11**, 2306424.



- 3 X. Li and Y. Chen, *J. Mater. Eng. Perform.*, 2021, **30**, 4819–4836.
- 4 J. T. Toombs, M. Luitz, C. C. Cook, S. Jenne, C. C. Li, B. E. Rapp, F. Kotz-Helmer and H. K. Taylor, *Science*, 2022, **376**, 308–312.
- 5 O. Dobre, M. A. G. Oliva, G. Ciccone, S. Trujillo, A. Rodrigo-Navarro, D. C. Venters, V. Llopis-Hernandez, M. Vassalli, C. Gonzalez-Garcia and M. J. Dalby, *Adv. Funct. Mater.*, 2021, **31**, 2010225.
- 6 N. Mamidi, F. Ijadi and M. H. Norahan, *Biomacromolecules*, 2024, **25**, 2075–2113.
- 7 S. M. Z. S. Bukhari, M. A. Bukhari and M. Hossain, *ACS Appl. Polym. Mater.*, 2025, **7**, 12117–12144.
- 8 F. Corrado, L. Di Maio, P. Palmero, B. Coppola, Z. Abbas, A. La Gatta, C. Schiraldi and P. Scarfato, *Acta Biomater.*, 2025, **200**, 67–86.
- 9 F. Wang, N. Cooper, Y. He, B. Hopton, D. Johnson, P. Zhao, C. J. Tuck, R. Hague, T. M. Fromhold, R. D. Wildman, L. Turyanska and L. Hackermüller, *Quantum Sci. Technol.*, 2025, **10**, 015019.
- 10 E. A. Recker, X. Chen, J.-W. Kim and Z. A. Page, *ACS Cent. Sci.*, 2025, **11**, 1527–1535.
- 11 Z. Xu, Z. Wu, Z. Xu and Q. Xu, *Front. Robot. AI*, 2024, **11**, 167390.
- 12 S. Subedi, S. Liu, W. Wang, S. M. A. Naser Shovon, X. Chen and H. O. T. Ware, *npj Adv. Manuf.*, 2024, **1**, 9.
- 13 K. Yue, G. Trujillo-De Santiago, M. M. Alvarez, A. Tamayol, N. Annabi and A. Khademhosseini, *Biomaterials*, 2015, **73**, 254–271.
- 14 S. Kumari, P. Mondal and K. Chatterjee, *Carbohydr. Polym.*, 2022, **290**, 119508.
- 15 K. Yu, X. Zhang, Y. Sun, Q. Gao, J. Fu, X. Cai and Y. He, *Bioact. Mater.*, 2022, **11**, 254–267.
- 16 M. Caprioli, I. Roppolo, A. Chiappone, L. Larush, C. F. Pirri and S. Magdassi, *Nat. Commun.*, 2021, **12**, 2462.
- 17 F. Puza and K. Lienkamp, *Adv. Funct. Mater.*, 2022, **32**, 2205345.
- 18 A. Agrawal and C. M. Hussain, *Gels*, 2023, **9**, 960.
- 19 M. A. Saccone, R. A. Gallivan, K. Narita, D. W. Yee and J. R. Greer, *Nature*, 2022, **612**, 685–690.
- 20 X. Xiong, Y. Chen, Z. Wang, H. Liu, M. Le, C. Lin, G. Wu, L. Wang, X. Shi, Y.-G. Jia and Y. Zhao, *Nat. Commun.*, 2023, **14**, 1331.
- 21 Y. Zhang and C. Wang, *MedComm: Biomater. Appl.*, 2022, **1**, e211.
- 22 G. Rivers, A. Lion, N. R. E. Putri, G. A. Rance, C. Moloney, V. Taresco, V. C. Crucitti, H. Constantin, M. I. E. Barreiros and L. R. Cantu, *Mater. Today Adv.*, 2024, **22**, 100493.
- 23 Y. He, M. Abdi, G. F. Trindade, B. Begines, J. Dubern, E. Prina, A. L. Hook, G. Y. H. Choong, J. Ledesma and C. J. Tuck, *Adv. Sci.*, 2021, **8**, 2100249.
- 24 A. Bastola, Y. He, J. Im, G. Rivers, F. Wang, R. Worsley, J. S. Austin, O. Nelson-Dummett, R. D. Wildman and R. Hague, *Mater. Today Electron.*, 2023, 100058.
- 25 S. Subedi, S. Liu, W. Wang, S. M. Abu, N. Shovon, X. Chen, H. Oliver and T. Ware, *npj Adv. Manuf.*, 2024, **1**, 9.
- 26 G. Fei, C. Parra-Cabrera, K. Zhong, K. Clays and R. Ameloot, *Adv. Funct. Mater.*, 2024, **34**, 2314635.
- 27 S. M. Montgomery, C. M. Hamel, J. Skovran and H. J. Qi, *Extreme Mech. Lett.*, 2022, **53**, 101714.
- 28 K. C. H. Chin, G. Ovsepyan and A. J. Boydston, *Nat. Commun.*, 2024, **15**, 3867.
- 29 J. Kim, S. A. Bencherif, W. A. Li and D. J. Mooney, *Macromol. Rapid Commun.*, 2014, **35**, 1578–1586.
- 30 M. Tromayer, A. Dobos, P. Gruber, A. Ajami, R. Dedic, A. Ovsianikov and R. Liska, *Polym. Chem.*, 2018, **9**, 3108–3117.
- 31 B. V. Derjaguin, V. M. Muller and Yu. P. Toporov, *J. Colloid Interface Sci.*, 1975, **53**, 314–326.
- 32 X. Zhang, W. Wu, Y. Huang, X. Yang and M. Gou, *Int. J. Bioprint*, 2023, **9**, 760.
- 33 K. Jodeiri, A. Foerster, G. F. Trindade, J. Im, D. Carballares, R. Fernández-Lafuente, M. Pita, A. L. De Lacey, C. D. Parmenter and C. Tuck, *ACS Appl. Mater. Interfaces*, 2023, **15**, 14914–14924.
- 34 R. Levato, K. S. Lim, W. Li, A. U. Asua, L. B. Peña, M. Wang, M. Falandt, P. N. Bernal, D. Gawlitta, Y. S. Zhang, T. B. F. Woodfield and J. Malda, *Mater. Today Bio*, 2021, **12**, 100162.
- 35 M. Nikkhah, M. Akbari, A. Paul, A. Memic, A. Dolatshahi-Pirouz and A. Khademhosseini, *Biomater. Nat. Adv. Devices Ther.*, 2016, **112**, 37–62.
- 36 T. Zandrini, S. Florczak, R. Levato and A. Ovsianikov, *Trends Biotechnol.*, 2023, **41**, 604–614.
- 37 R. G. M. Breuls, T. U. Jiya and T. H. Smit, *Open Orthop. J.*, 2008, **2**, 103–109.
- 38 M. Sun, X. Sun, Z. Wang, S. Guo, G. Yu and H. Yang, *Polymers*, 2018, **10**, 1290.
- 39 R. Fagotto-Clavijo, I. Lodoso-Torrecilla, A. Diez-Escudero and M.-P. Ginebra, *Bioact. Mater.*, 2025, **52**, 719–752.
- 40 K. Zöller, D. To and A. Bernkop-Schnürch, *Biomaterials*, 2025, **312**, 122718.
- 41 M. Vigata, C. Meinert, D. W. Huttmacher and N. Bock, *Pharmaceutics*, 2020, **12**, 1188.
- 42 D. Magde, E. L. Elson and W. W. Webb, *Biopolymers*, 1974, **13**, 29–61.
- 43 A. Bernal, M. A. Zafra, M. J. Simón and J. Mahía, *Nutrients*, 2023, **15**, 395.
- 44 M. A. Zoroddu, J. Aaseth, G. Crisponi, S. Medici, M. Peana and V. M. Nurchi, *J. Inorg. Biochem.*, 2019, **195**, 120–129.
- 45 B. Sapotta, M. Schwotzer and M. Franzreb, *Electroanalysis*, 2023, **35**, e202200102.
- 46 L. Yang, A. Guiseppi-Wilson and A. Guiseppi-Elie, *Biomed. Microdevices*, 2010, **13**, 279–289.
- 47 G. M. Fernandes-Cunha, K. M. Chen, F. Chen, P. Le, J. H. Han, L. A. Mahajan, H. J. Lee, K. S. Na and D. Myung, *Sci. Rep.*, 2020, **10**, 16671.
- 48 J. He, Y. Sun, Q. Gao, C. He, K. Yao, T. Wang, M. Xie, K. Yu, J. Nie, Y. Chen and Y. He, *Adv. Healthcare Mater.*, 2023, **12**, 2300395.
- 49 H. Yilmaz, S. Gursoy, H. Calik, Y. Kazancioglu, R. Yildirim, R. Cakir, O. Gunduz, A. Ahmed and C. B. Ustundag, *Mater. Res. Express*, 2024, **11**, 075307.

